Stroboscopic microwave spectroscopy of Voigt-based optically pumped magnetometers

Hans Marin Florez [1], Tadas Pyragius [2,3] and Thomas Fernholz [2]

[1]*Instituto de Física, Universidade de São Paulo, 05315-970 São Paulo, São Paulo, Brazil*

[2]*School of Physics & Astronomy, University of Nottingham, University Park, Nottingham NG7 2RD, United Kingdom*

[3]*Tokamak Energy Ltd, Milton Park, Oxfordshire OX14 4SD, United Kingdom*

(Received 25 October 2023; revised 8 May 2024; accepted 13 September 2024; published 1 October 2024)

We present the results of stroboscopic microwave spectroscopy of a radio-frequency-dressed optically pumped magnetometer. The interaction between radio-frequency-dressed atoms and a synchronously pulsed microwave field followed by Voigt-effect-based optical probing allows us to perform a proper ground-state interrogation for dressed state and assess the efficiency of the state preparation process. This work shows that through the stroboscopic technique the microwave spectrum is simplified when compared to the continuous counterpart. This is a necessary step towards investigating vector magnetometers in unshielded environments, where the influence of the nonlinear Zeeman effect, a source of heading errors, would otherwise be spectrally unresolved in dressed states. To theoretically describe the system, we solve the dynamical equation of the density matrix employing Floquet expansion. Our theoretical results are in good agreement with experimental measurements over a wide range of parameters and pumping conditions.

DOI: 10.1103/PhysRevA.110.043102

I. INTRODUCTION

Atomic-vapor-based optically pumped magnetometers (OPMs) [1,2] have become the state-of-the-art devices for highly sensitive magnetic-field detection reaching $\mathrm{fT}/\sqrt{\mathrm{Hz}}$ sensitivities and beyond. During the past decade OPMs found applications across many domains from fundamental physics, e.g., in the search for electric dipole moments [3,4], in geophysical and space magnetometry, and in medical applications, such as magnetoencephalography [5,6] and magnetocardiography [7–9]. A commonly used OPM architecture is based on Faraday rotation, which further exploits the spin-exchange relaxation-free regime [10,11]. In such setups, the atoms are prepared in a spin-polarized state such that in the presence of a magnetic field their precession can be detected by measuring the Faraday rotation through light-matter interaction between the atoms and a probe beam, operating as a scalar magnetometer. However, for unshielded applications, atomic magnetometers are subjected to heading errors due to nonlinear Zeeman (NLZ) shifts and ground-state population distribution. The combination of such effects makes the measurement of the magnetic fields dependent on the angle between the pump and the target magnetic field, leading to a different reading of the target field [12].

In order to mitigate the heading error in scalar magnetometers in unshielded environments, different strategies have been recently proposed, such as a pulse pump for high spin polarization [13], spin locking applying radio-frequency fields [14], and alignment resonance [15], among others. In the case of a pump pulse for high spin polarization, for atoms with ground hyperfine levels $F = I \pm 1/2$, if the atoms remain in $F = I + 1/2$, which means spin polarization $P \approx 1$, the precession is less sensitive to heading errors. Operating at low spin polarization $P \approx 0.5$ enhances the asymmetries of the ground-state distribution and makes it susceptible to the NLZ effect. In the case of spin locking by applying an rf field, the ground-state population becomes symmetric, making it more robust against orientation changes. A similar effect is obtained by using linear polarization with aligned states. Consequently, systems like M_x magnetometers [16–18], double resonance magnetometer [19], or more recently the rf-dressed state utilizing the aligned states [20] are robust against heading errors due to NLZ shifts or asymmetric ground-state populations [14]. Still, in all those cases, interrogating the ground-state population is a proper strategy to identify the effect of heading error.

Therefore, tools for interrogation of the state preparation are important to verify high sensitivity in shielded systems and determine how the heading error affects the ground-state distribution in unshielded conditions. For scalar magnetometers, microwave (MW) fields have been employed [21] to observe population distribution through Rabi oscillations and NLZ shifts, as in Ref. [22] for nondressed states through Rabi and Ramsey microwave spectroscopy. Asymmetries in the ground-state populations can be verified using conventional MW spectroscopy [23] with a circularly polarized probe beam. However, in the case of vector magnetometers, measuring such asymmetry or the effect of NLZ shifts is not straightforward. Measuring the misalignment between the total magnetic field and the pump axis to extract the components of the magnetic field is the goal in such kinds of magnetometers. The misalignment leads to the asymmetric distribution either by NLZ shift or as a response to the vector orientation. Therefore, interrogating the ground-state distribution in a vector magnetometer is not a straightforward task.

That is the case of the recent Voigt-effect rf-dressed-based vector magnetometer we proposed in Ref. [20]. The Voigt effect is due to linear birefringence arising from aligned rather than oriented spin states. In this system, sensitive field measurements are achieved by preparing an aligned state in the presence of a longitudinal magnetic field and an additional

rf-dressing field. Such a state can, e.g., be prepared as an equal statistical mixture of two stretched states or as an $m = 0$ state. The rf field drives the state precession, producing two harmonics in the ellipticity of the output signal. The quadratures of the first harmonic map the transverse fields, and the second harmonic maps the longitudinal field. This way, the Voigt rotation allows vector magnetometer operation. This kind of system leverages the use of spin-polarized samples ($P \sim 1$), aligned states, and rf fields, making it robust against heading errors due to NLZ shifts and ground-state asymmetries [13–15]. As in the case of scalar magnetometers, the ground-state distribution of such an aligned state in the vector magnetometer can be interrogated by standard microwave spectroscopy [21]. However, when atoms are additionally driven by an rf field, the Zeeman levels are dressed and the standard selection rules no longer apply. This gives rise to a rich MW spectrum, significantly increasing the number of resonant lines, making it difficult to infer the prepared state, as shown in Ref. [24]. Alternatively, one can employ a magneto-optical resonance signal to probe the energy-level distribution [25]. However, this requires driving the system to a nonlinear magnetic regime, which would destroy the target state that is aimed to be prepared. Hence, an alternative nondestructive technique is required to interrogate the ground-state distribution in vector magnetometers, particularly when the state is dressed by rf fields.

Inspired by previous work in [24], we propose a method of stroboscopic microwave spectroscopy which enables the interrogation of the population distributions of the prepared atomic states in a dressed scenario in a linear magnetic regime and via Voigt rotation. Furthermore, we demonstrate how the synchronous detection allows us to measure the subtle differences in the state preparation with high ($P \sim 1$) and low ($P < 1$) spin-polarized samples, with the use of a repump beam. Building upon our previous theoretical work employing the Floquet expansion on second-order moments, we extend our theoretical analysis to the density matrix in order to calculate the microwave spectra [26]. Using this technique in an unshielded situation along with our theoretical model, we are able to determine our target state and estimate the efficiency of the state preparation process reaching more than 90%. We find that our theoretical description is effective in understanding the experimental results. This nondestructive technique is an intermediate step towards characterizing the effect of heading error in vector magnetometers.

The paper is organized as follows. In Sec. II we briefly describe the spin dynamics and introduce the Floquet expansion to describe the microwave spectroscopy. Section III presents the experimental setup and the experimental sequence used to realize the synchronous microwave spectroscopy. Section IV shows the experimental and theoretical results on continuous microwave spectroscopy, whereas Sec. V shows the results on the synchronous stroboscopic microwave spectroscopy for Voigt-effect-based OPMs. Section VI presents a summary and our conclusions.

II. MICROWAVE SPECTROSCOPY PROBED BY VOIGT ROTATION

The experiments carried out in this work are based on a Voigt-effect OPM using radio-frequency-dressed states (see Ref. [20] for further details). The Voigt rotation for linearly polarized light is due to the linear birefringence induced by the magnetization of a medium, in this case, the atomic spins, aligned in the same plane as the light polarization. The light-matter interaction for such rotation is described by the Stokes parameter

$$\langle \hat{S}'_z(t)\rangle = \langle \hat{S}_z(t)\rangle + G_F^{(2)} S_y n_F \left\langle \hat{F}_x^2(t) - \hat{F}_y^2(t)\right\rangle, \tag{1}$$

where $\hat{S}_z = (c/2)(\hat{a}_+^\dagger \hat{a}_+ - \hat{a}_-^\dagger \hat{a}_-)$ and $\hat{S}_y = (c/2)(i\hat{a}_-^\dagger \hat{a}_+ - i\hat{a}_+^\dagger \hat{a}_-)$ represent the photon flux differences in a circular and a 45° polarization basis, respectively, $G_F^{(k)}$ is the rank-k coupling strength, and n_F is the number of atoms within the same F-manifold state [27]. In terms of the Stokes parameters, the Voigt effect is a rotation from linear to elliptical polarization on the Stokes sphere. The angle of rotation is proportional to $\langle \hat{F}_i^2\rangle$, which is nonzero for aligned states, instead of a Faraday rotation proportional to $\langle \hat{F}_z\rangle$, which is nonzero for oriented states. The nonlinearity of the spin signal is a key feature for vector magnetometer operation.

In the presence of the static field $B_{\rm dc}$ and the rf-dressing field $B_{\rm rf}$, the slow field interaction is $\hat{H}_B = (\mu_B g_F/\hbar)\hat{\mathbf{F}}\cdot\mathbf{B}$, where μ_B and g_F correspond to the Bohr magnetron and g_F factor, respectively. The total magnetic fields is

$$\mathbf{B} = \left(B_{\rm rf}\cos\omega_{\rm rf}t + B_x^{\rm ext}\right)\mathbf{e}_x + B_y^{\rm ext}\mathbf{e}_y + \left(B_{\rm dc} + B_z^{\rm ext}\right)\mathbf{e}_z, \tag{2}$$

where $\omega_{\rm rf}$ corresponds to the frequency of the rf field, and we consider the general case in which external fields $\mathbf{B}^{\rm ext} = (B_x^{\rm ext}, B_y^{\rm ext}, B_z^{\rm ext})$ are present. By applying the rf field, the static field $B_{\rm dc}$ tunes the spin precession oscillating at $\omega_{\rm rf}$ such that $\hat{F}_x$ represents only one oscillating term proportional to $e^{i\omega_{\rm rf}t}$. The ellipticity from Eq. (1), which is proportional to $\langle \hat{F}_x^2\rangle$, represents two oscillating terms proportional to the first harmonic $e^{i\omega_{\rm rf}t}$ and second harmonic $e^{2i\omega_{\rm rf}t}$. Thus, the ellipticity represents two harmonic terms, where the quadratures of the first harmonic map the presence of the transverse fields and the second harmonic maps the longitudinal field. Such spectral decomposition allows us to extract the three components of the magnetic field. The amplitude of the harmonics is maximized when the Larmor frequency of the static field tunes the magnetic resonance given by $\Delta_{\rm rf} = \mu_B g_F B_{\rm dc} - \omega_{\rm rf}$. The details of this harmonic decomposition are presented in Appendix A 4.

In order to properly describe the ground-state interrogation through the first and second harmonics of the Voigt rotation in Eq. (1), we make the atoms interact with a microwave magnetic field, aiming to obtain the MW spectrum of the prepared state. The MW-field interaction is theoretically described by considering alkali-metal atoms in the ground state ${}^nS_{1/2}$, where the orbital angular momentum is $L = 0$, allowing an approximation $\hat{\mathbf{J}} = \hat{\mathbf{L}} + \hat{\mathbf{S}} \approx \hat{\mathbf{S}}$. Specifically, we consider ^{87}Rb atoms with hyperfine ground states $F = 1$ and $F = 2$. By neglecting the nuclear magnetic moment since it is much smaller than the electronic one, i.e., $g_I\mu_B \ll g_S\mu_B$, the microwave interaction Hamiltonian reduces to $\hat{H}_{\rm MW}(t) = (\mu_B g_S/\hbar)\hat{\mathbf{S}}\cdot\mathbf{B}_{\rm MW}(t)$ and can be effectively expressed as

$$\hat{H}_{\rm MW}^{\rm eff} = \hat{\mathbf{H}}_0 + \Omega_\pi \hat{S}_z + \Omega_{\sigma+}\hat{S}_{\sigma+} + \Omega_{\sigma-}\hat{S}_{\sigma-}, \tag{3}$$

where $\hat{\mathbf{H}}_0$ carries the detuning $\Delta = \omega_{\rm MW} - \omega_{\rm hfs}$ of the microwave field with frequency $\omega_{\rm MW}$ with respect to the

hyperfine energy levels $\omega_{\rm hfs}$. The detailed definition of $\hat{\mathbf{H}}_0$ and the spin operators are defined in Eqs. (A12)–(A16). The dynamics describe the Rabi oscillations induced by the microwave field $\hat{\mathbf{S}}_i$ coupling the two hyperfine ground states of alkali-metal atoms. The details are presented in Appendix A 1.

Hence, the total coherent dynamics is given by $\hat{H}_T(t) = \hat{H}^{\rm eff}_{\rm MW} + \hat{H}_B(t)$, which considers the fast interaction with the MW field that induces transitions among the ground hyperfine levels and the slow interaction that drives the spin state, modulating the ellipticity in Eq. (1). Including the pumping rate $\Gamma_p(t)$, which allows the state preparation with an arbitrary time profile, and the relaxation rate γ due to collisions, the total dynamics of the atomic state $\rho(t)$ can be described by

$$\frac{d\tilde{\rho}}{dt} = \frac{i}{\hbar}[\tilde{\rho}, \hat{H}_T(t)] - \Gamma_p(t)(\tilde{\rho} - \rho_{in}) - \gamma(\tilde{\rho} - \rho_0). \quad (4)$$

defined in Appendix A 2, where ρ_{in} is the state prepared by optical pumping whereas ρ_0 is the thermal state due to relaxation processes. These dynamics equations describe both situations we aim to study in this work: one in which the MW field is a continuous wave and another in which we strobe the MW field synchronously with the rf-field phase. Solving the dynamics in a general situation where the pumping rate and the microwave fields are modulated with an arbitrary time profile at a frequency $\omega_{\rm rf}$ is not straightforward. However, by applying the Floquet expansion to the density operator, as in Ref. [26], it is possible to find a steady-state solution. Considering a harmonic expansion of the density-matrix elements as $\rho_{ij}(t) = \sum_n \rho^{(n)}_{ij}(t)e^{in\omega_{\rm rf}t}$, with $n \in Z$, it is possible to find the steady-state solution of the harmonics $\rho^{(n)}_{ij}(t)$, which is described in detail in Appendix A 3.

III. EXPERIMENTAL SETUP

Our magnetically unshielded experimental setup is depicted in Fig. 1 and its detailed description is presented in Appendix B. It follows closely the shielded version of the experimental setup described in Ref. [20]. It consists of a paraffin-coated ^{87}Rb enriched vapor cell at room temperature [see Fig. 1(a)]. The atoms are dressed with an $\omega_{\rm rf} = 2\pi \times 90$ kHz rf field in the x direction and coupled to a static field in the longitudinal direction. Three pairs of Helmholtz coils are used to actively compensate and stabilize the external magnetic field. The atomic state is prepared by a pump laser beam tuned to the $F = 2$ to $F' = 1$ transition of the $D1$ line. The atoms are stroboscopically pumped by modulating the pump amplitude with 10% duty cycle in phase with the rf field.

After the state preparation the atoms are interrogated with the MW field in a continuous or pulsed configuration. To probe the state precession, we employ the Voigt rotation for nondestructive measurements in hyperfine ground states $F = 1$ and $F = 2$ [see Fig. 1(b)]. The light is detected on a balanced photodetector where the detected signal $u(t) = g_{\rm el}S_z(t)$ is proportional to the ellipticity in Eq. (1) and the electronic gain $g_{\rm el}$. As it was shown in Ref. [20], the ellipticity for the Voigt rotation produces a signal at the first and second harmonics of the radio-frequency-dressing field such that $u(t) = m_0 + m_1e^{i\omega_{\rm rf}t} + m_2e^{2i\omega_{\rm rf}t} + {\rm c.c.}$ This output signal

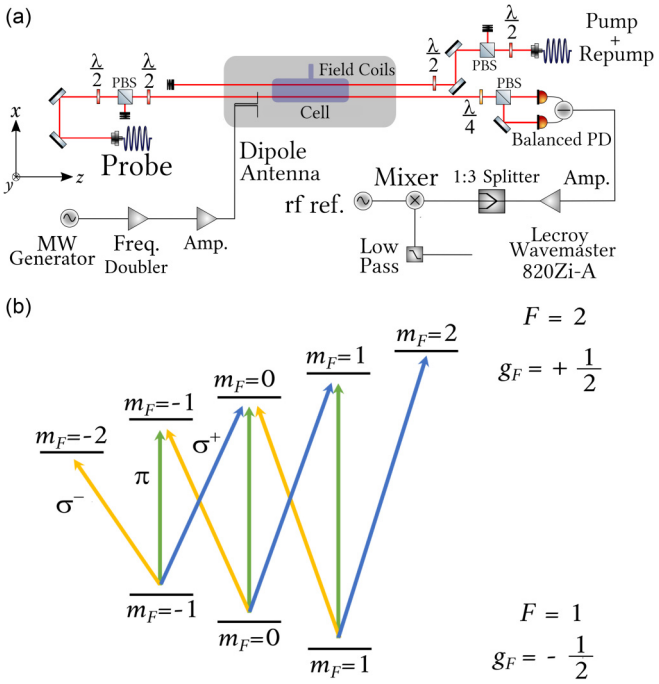

FIG. 1. (a) Sketch of the experimental setup. (b) Bare Zeeman states of ^{87}Rb and polarizations of MW transitions.

is demodulated at the second harmonic, from which we can extract its mode amplitude m_2. The microwave spectroscopy is performed with the magnetometer tuned on resonance, $B_{\rm dc} = \hbar\omega_{\rm rf}/\mu_B g_F$ using the second rf harmonic in the Voigt rotation signal, canceling the presence of any transverse field, i.e., zeroing the first harmonic [20]. The direction of the dipole antenna is transversal to the light propagation [see Fig. 1(a)].

The time sequence to obtain the MW spectroscopy is shown in Fig. 2. First, we prepare the atomic state through the interaction with the pump and rf field. Then we have the stage of the microwave interaction and finally we probe the atomic state. The microwave interaction is done continuously or stroboscopically, which give rise different results.

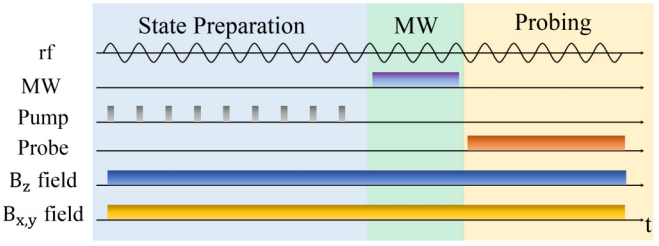

FIG. 2. Sequence to produce the MW spectroscopy. The sequence is composed of three separate stages. First the process is initiated by the state preparation process where the rf-dressed atoms are synchronously pumped to prepare an aligned state. This is then followed by switching all of the optical fields off and applying a short MW pulse tuned to the ground hyperfine splitting to induce a population transfer. The atomic dynamics are then probed by an off-resonant probe beam to measure the Voigt effect.

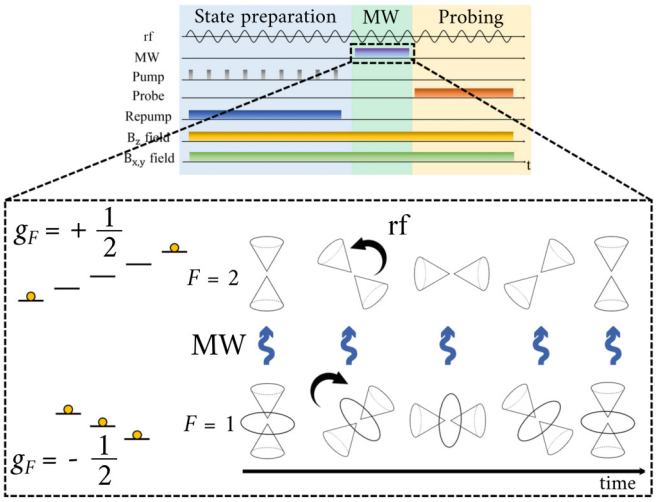

FIG. 3. Illustration of the experimental sequence and the microwave coupling of the ground-state manifolds in the continuous-wave model. The sequence consists of three separate stages: state preparation, microwave interaction, and probing. The states in each manifold rotate in opposite directions due to the different g_F factors. The microwave radiation transfers the state populations between the two energy levels at different cone orientations during the evolution.

IV. RESULTS FOR CONTINUOUS MICROWAVE SPECTROSCOPY

We first perform continuous-wave (cw) microwave spectroscopy during the relaxation dynamics of the prepared state, as it is shown in Fig. 3(a). For a microwave field composed of $\sigma^{\pm}$ and π polarizations applied to $F = 1 \rightarrow F = 2$ in the presence of an external static magnetic field, there is a total of nine possible microwave transitions, four of which are degenerate [see Fig. 1(a)]. This results in seven distinct resonance peaks in the undressed microwave spectrum when the microwave field frequency is scanned (assuming a thermal state in each manifold), separated by $\Delta\omega = \mu_B g_F B_{\rm dc}/\hbar$. If the state is polarized, e.g., we have a stretched state, then only one transition will be observed. If, as in our case, an equal statistical mixture $|F = 2, m_F = \pm 2\rangle$ is prepared, then the two extreme transitions should be observed.

Now, in the case of rf-dressed states, the spectrum includes new transitions in the dressed basis. Figure 4 shows theoretical and experimental rf-dressed microwave spectra of the Re(m_2) demodulated signal amplitude for $F = 2$ manifolds for two differently prepared states. As described in [24], the general structure of these spectra comprises seven groups of up to seven lines. Different groups are addressed by different MW polarizations, but the complete set arises here due to the inhomogeneous field distribution from the dipole antenna. The group structure resembles that of bare transitions, alternating between π and σ polarizations, with a spacing given the static field strength. Lines within a group are spaced by approximately $\sqrt{\Omega_{\rm rf}^2 + \Delta_{\rm rf}^2}$. Since in our case the static field is in resonance with the Zeeman levels, $\Delta_{\rm rf} = 0$, the line spacing measures the rf amplitude, since $B_{\rm rf} = \hbar\Omega_{\rm rf}/\mu_B g_F$. This can be used to obtain absolute field values for both the static and rf fields, which provides a method for absolute ac and dc field calibrations.

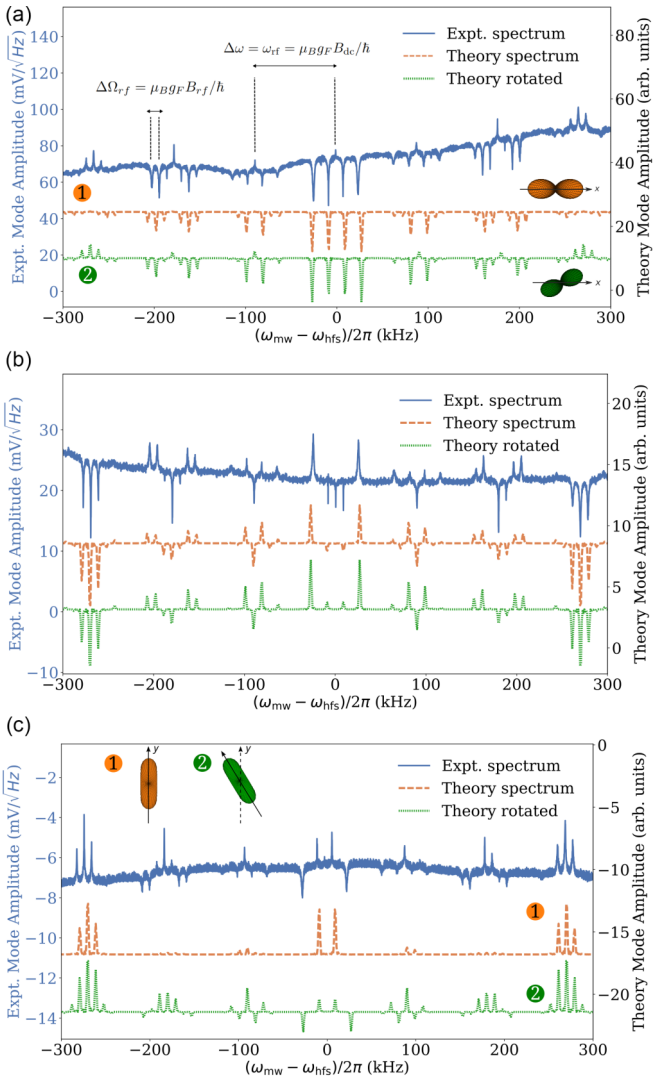

FIG. 4. Experimental (blue top line) and theoretical (curve 1, orange middle dashed line) dressed microwave spectra of the Re(m_2) mode amplitude as a function of the microwave frequency. Here the measured and calculated spectra are obtained based on the sequence in Fig. 3. The probe beam interacts from $F = 2$ to the excited states, when the MW is a cw with (a) an aligned stretched state with the repump on and (b) the repump off and (c) the $|m = 0\rangle_x$ state repump on. Here the theoretical MW is applied in a cw mode over 20 rf periods $T = 2\pi/\omega_{\rm rf}$. In both cases we considered an effective rotation of approximately 35° plotted in curve 2 (green bottom dotted line).

A. Microwave spectroscopy probing the $F = 2$ state

Figure 4(a) displays data obtained with repump light, which is used to prepare a highly polarized sample ($P \approx 1$). This sample is intended to create a mixture of the two rf-dressed fully stretched states. Here population that leaks into the $F = 1$ manifold is redistributed onto the $F = 2$ manifold, where it interacts with the pump beam, thus approaching $P \approx 1$. This results in a zero birefringence signal in the $F = 1$ manifold and nonzero birefringence in the $F = 2$ manifold, which is seen as a large offset in the data. The prepared state is close to maximal birefringence and any coupling of the $F = 1$ and $F = 2$ manifolds by resonant microwave transitions

alters state populations and becomes visible mostly as spectral dips. However, the rf-dressed microwave spectrum possesses a complex and difficult to interpret structure compared to a bare spectrum. This is because the rf radiation provides additional coupling within the Zeeman states corresponding to coherences in the density matrix which contain information about the correlations between any two given populations. If the MW field is turned on all the time, then the evolution of the MW field and the state is averaged, i.e., different relative orientations between the cones end up contributing to the overall spectrum, as it is shown in Fig. 3(b). The coupling of the MW field from one manifold to the other probes the orientation of those two cones relative to each other as the MW-field frequency is continuously scanned. This allows the probing of all the possible transitions resulting in a dense forest of lines, rendering the standard selection rules obsolete. For example, coupling $|F = 1, m_F = -1\rangle$ and $|F = 2, m_F = 2\rangle$ is possible. Hence, the addition of the rf-dressing field gives rise to partially degenerate multiphoton transitions, enabling the coupling between any two given states [24].

Now let us consider the situation in Fig. 4(b), which shows microwave spectra of the OPM without the repump, for the Voigt rotation in $F = 2$. If the repump is turned off a fraction of the population is pumped into $F = 1$ and another fraction remains in $F = 2$ such that $P < 1$. Still, the pump beam drives the atoms to an aligned state with lower efficiency. Unlike in the previous case, the $F = 1$ manifold is now populated but is in a near-thermal state with vanishing birefringence, which strongly diminishes the $\mathrm{Re}(m_2)$ offset amplitude. Nevertheless, here the microwave coupling between the two ground-state manifolds enables a two-way population exchange, which is distinct from the previous case. The MW transitions may now change birefringence in either sense. Still, the MW spectrum is changed with respect to the spin-polarized case $P \approx 1$ in Fig. 4(a).

Another situation we can explore is the case where the pump couples the $F = 2 \rightarrow F' = 2$ transition, which prepares the dressed $|F = 2, m = 0\rangle_x$ state, referred to as $|m = 0\rangle_x$ throughout the paper. Figure 4(c) shows the MW spectra for the dressed $|m = 0\rangle_x$ with the repump on to keep the sample polarized $P \approx 1$. In this case the state, represented as a torus density surface, is rotated 90° with respect to the aligned stretched state of Fig. 4(a). This leads to a negative sign on the mode amplitude $\mathrm{Re}(m_2)$ since $\langle F_x^2 \rangle < \langle F_y^2 \rangle$.

For further discussion, we focus on the $F = 2$ manifold, where we prepare the atomic aligned state. In this case, curves labeled 1 and 2 correspond to the theoretical MW spectrum, which displays a structure similar to the experimental one, with some differences. In particular, for the case of active repumping in Fig. 4(a), curve 1 shows that the two extreme groups are clearly different from the experimental observations, whereas for the case of no repumping in Fig. 4(b), the same groups are properly described.

This state dependence can be related to an interaction with an optically thick medium, leading to propagation effects of the pump field on the state preparation process. In the case of $F = 2$ with the repump on, the atomic density is optically thick enough to produce a polarization rotation on the pump field around the z axis of propagation through a nonlinear magneto-optical rotation (NMOR) due to the presence of the

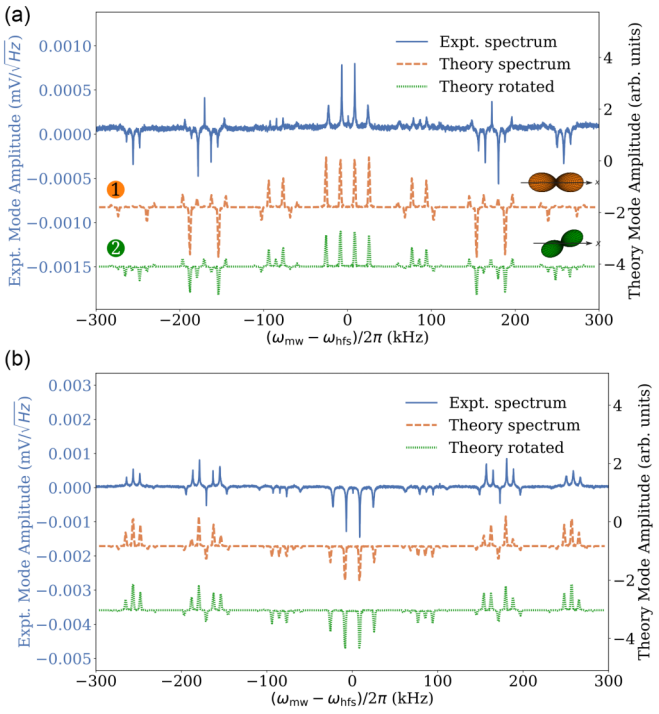

FIG. 5. Experimental (blue top line) and theoretical (curve 1, orange middle dashed line) dressed microwave spectra of the $\mathrm{Re}(m_2)$ mode amplitude probing the $F = 1$ manifold following the sequence in Fig. 3 with (a) repump on and (b) repump off. In both cases we considered an effective rotation of 35° plotted in curve 2 (green bottom dotted line).

static field B_{dc} [28]. This rotation can effectively produce a stretched aligned state rotated with respect to the z axis as the pump field propagates through the medium. By introducing the effective rotation in the prepared state, emulating the rotation experienced by the pump field, we find that an angle of approximately 35° fits the experimental observations.[1] Considering this effective rotation, curve 2 is now in agreement with experimental observations. The effective rotation of the prepared state is detailed in Appendix C. This is not the case for the spectrum in Fig. 4(b), where applying the same rotation effect does not change the extreme group profiles but instead modifies the central group. This indicates that without the repump, the atomic $F = 2$ population is low compared to the case with an active repump, and no propagation effects need to be considered.

A similar situation occurs with $|m = 0\rangle_x$. The microwave spectrum in Fig. 4(c) is also subjected to propagation effects, as shown by curves 1 and 2, which show that the model presents a better description of the MW spectroscopy when the effective rotation in curve 2 is considered.

B. Microwave spectroscopy probing the $F = 1$ state

Complementing the observations of the MW spectroscopy when we probed the state $F = 2$, in this section we present the

[1]The full calculation of a NMOR for the exact atomic transitions used in the experiment, considering the actual propagation through a thick medium, is beyond the scope of this paper.

cw MW spectroscopy when the $F = 1$ manifold is probed. Figure 5(a) shows the MW spectrum when the repump is on during the pumping process, which polarizes the sample $P \approx 1$. It is worth noting that the birefringent signal mean value is around zero since its population is empty and initially prepared in $F = 2$. Figure 5(b) shows the case when the repump is off ($P < 1$) such that the birefringent signal acquires opposite polarity, since the residual population in $F = 1$ can now be excited to the $F = 2$ ground state.

As in the case of probing the state $F = 2$, the MW spectroscopy shows a dressed spectrum, from which we cannot extract information of the state that is prepared in the bare basis. Nevertheless, it is possible to observe that ground-state population for $F = 1$ is the complement of $F = 2$ such that a dip (loss of population) in the $F = 2$ spectrum corresponds to a peak (gain of population) in the $F = 1$ spectrum and vice versa. In the central group, for instance, Fig. 5(a) shows that the sample is polarized $P \approx 1$ and $F = 1$ only gains population from the $F = 2$ state represented by the peaks where the birefringence increases. On the other hand, Fig. 5(b) shows a sample with low polarization $P < 1$ such that the microwave field induces a transition reducing the population in $F = 1$ represented by the dips.

Similarly to the case of probing $F = 2$, in this case the propagation effects are also present in the pump-atom interaction, degrading the efficiency of the state preparation process. Note that in the case when the repump is on, the extreme group describes the populations observed experimentally, whereas for the case of no repump, the correction with the rotation does not appear to change the profile.

V. RESULTS FOR STROBOSCOPIC MICROWAVE SPECTROSCOPY

Although Figs. 4 and 5 demonstrate changes in the prepared state, whether aligned, stretched, or $|m = 0\rangle_x$, observable in the microwave spectroscopy, inferring population distributions in the rf-dressed picture (i.e., the quasienergy eigenstates) is not straightforward. Consequently, an alternative probing scheme is necessary. We propose an rf-synchronized stroboscopic microwave probing scheme to map population distributions in the presence of an rf-dressing field.

A. Microwave spectroscopy probing the $F = 2$ state

Figure 6(a) shows the results of a pulsed microwave spectrum of Re(m_2) probing the $F = 2$ ground-state manifold, for the situation analyzed in Fig. 4(a) when the repump is active. Here the microwave field is pulsed with the same duty cycle of 10% and in phase with the rf-dressing field, as it is shown in Fig. 7(a). The experimental stroboscopic microwave spectrum shows mainly two peaks per group which lie on the two extreme edges. However, some of the manifold populations leak into the inner levels. On the other hand, curve 1 represents the theoretical calculation. It shows that when the system is prepared in an equal statistical mixture of the stretched states and then probed stroboscopically using MW radiation in phase with the rf-dressing field, the atomic populations are perfectly distributed into two extreme peaks in the dressed microwave

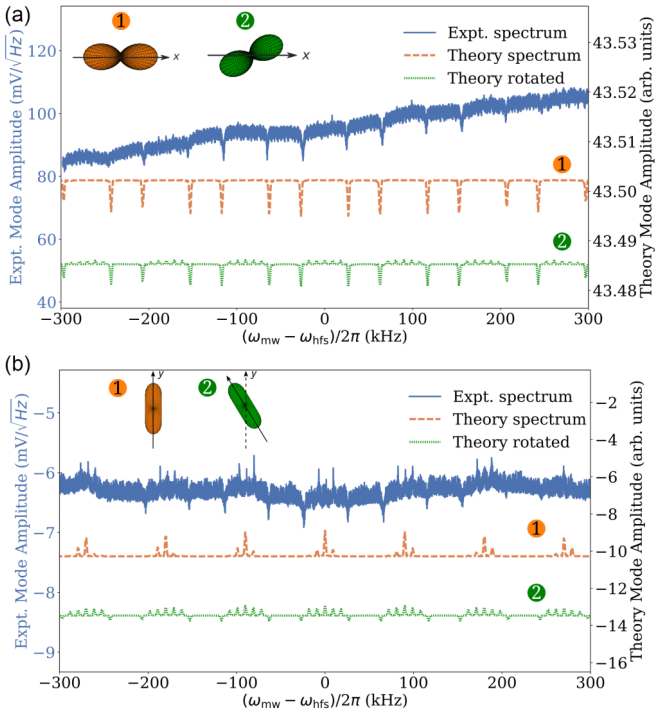

FIG. 6. Experimental (blue top line) and theoretical (curve 1, orange middle line) dressed microwave spectra of the Re(m_2) mode amplitude as a function of the microwave detuning with respect to the clock transition. Here the measured and calculated spectra are obtained based on the sequence in Fig. 7 where the MW is pulsed. (a) Aligned state with repump on and (b) $|m = 0\rangle_x$ with repump on. In both cases we considered an effective rotation of approximately 35° plotted in curve 2 (green bottom line).

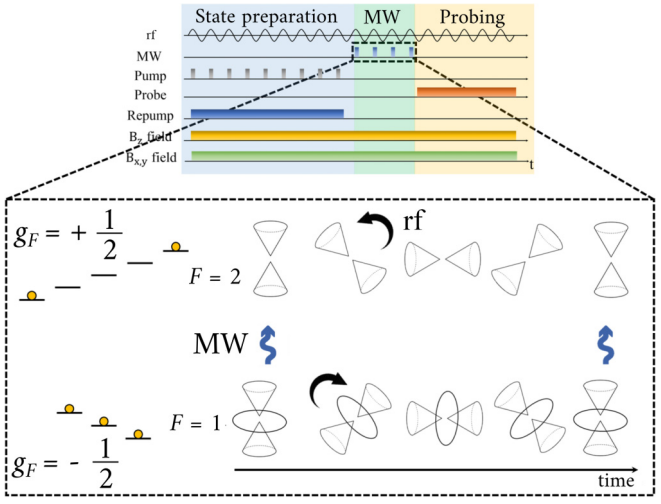

FIG. 7. Illustration of the experimental sequence and the microwave coupling of the ground-state manifolds during stroboscopic microwave probing. Here the states in each manifold are probed only at a specific time (stroboscopic microwave interaction), which means that the population transfer between the two levels happens only at a certain orientation between the two cones. The microwave pulses are in phase with the rf field.

spectrum, repeated over the seven groups.[2] This is expected for an aligned state, in which the majority of the populations resides in the Zeeman sublevels of the $|F = 2, m_F = \pm 2\rangle$ mixed state along the x axis. Now the inner peaks detected on the MW scan can be described by taking into account the propagation effect as in Fig. 4. Note that if we consider some effective rotation due to the propagation effects, the resultant theoretical spectrum in curve 2 matches the experimental observations, showing the presence of the inner peaks. This indicates that without propagation effects our state preparation process can in principle reach near-perfect efficiency with the atoms ending up in the target state. However, when the propagation effects are considered, the aligned state is rotated, thus reducing the preparation efficiency to approximately 70% of the mixture of the two stretched states.

Therefore, these results demonstrate an important aspect of stroboscopic spectroscopy: the simplification of the dressed spectrum to resolve any new spectral lines when the system is subjected to a larger magnetic field, resulting in a NLZ shift. In the cw spectroscopy in Fig. 4(a), except for the central group, most groups present loss and gain of population (dips and peaks) due to the dressed state. However, mapping the spectral lines to bare atomic populations is not a straightforward task. Inferring any asymmetry in the population distribution or the line spacing is challenging. Conversely, stroboscopic spectroscopy simplifies the spectrum, allowing us to determine if the atomic population is symmetric. Modifications in the line spacing or new peaks would be more easily observed than in the continuous spectrum. Although this work does not address the nonlinear Zeeman effect on dressed states, this simplification through stroboscopic measurements is a step towards a proper investigation of the NLZ effect with dressed states in a vector magnetometer.

Now, in order to describe how the stroboscopic spectroscopy captures the target state that we aim to prepare, we analyze the time evolution of the atomic state with the timing of the microwave. This stroboscopic MW spectrum measurement can be described as probing the states at a certain orientation in their evolution as they precess around the static and rf fields (see Fig. 7). As a result, when the MW field is pulsed and its frequency scanned, only a certain part of the cone configuration is probed and so the spectrum acquires only the shape of the corresponding bare spectrum, or rather the spectrum is obtained based on a single orientation of the cones.

To further test the efficacy of our theoretical model, we analyze the stroboscopic MW spectrum for a dressed $|m = 0\rangle_x$ state, shown in Fig. 6(b). In this case, one can notice that the state preparation produces not just the $|m = 0\rangle_x$ state, but a distribution within the manifold. Once again, the theoretical model shows that if the input state corresponds to an $|m = 0\rangle_x$ state in the x direction (curve 1), the stroboscopic spectrum should be mainly determined by the $|m = 0\rangle_x$ state. However, when considering the propagation effects (curve 2), the model predicts the population distribution to the one

[2]The multiple reproduction of the single dressed MW spectrum is due to the harmonics generated by the square modulation of the MW field.

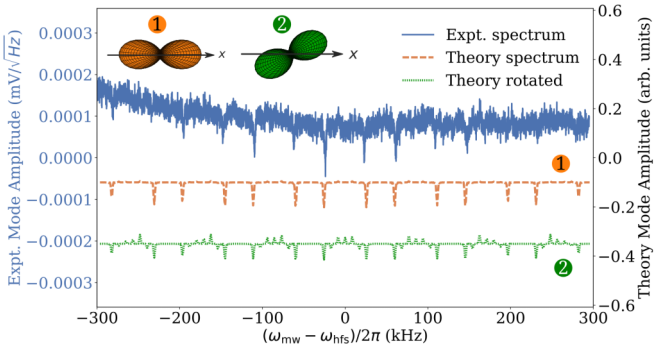

FIG. 8. Experimental (blue top line) and theoretical (curve 1, orange middle line) dressed microwave spectra of the Re(m_2) mode amplitude for a synchronous MW interaction for the aligned streched state. Curve 2 (green bottom dashed line) correspond to an effective rotation of apporximatly 35° with respect to atomic state in curve 1.

observed experimentally. This shows that the $|m = 0\rangle_x$ state can be more sensitive to propagation effects than the aligned stretched state. On the other hand, despite the reduction of the signal-to-noise ratio of Fig. 6(b) with respect to Fig. 6(a), there is a clear difference in the profile for most of the groups of the stroboscopic measurement when compared to the cw MW spectrum in Fig. 4(c). This can be observed in groups 2, 3, 5, and 6, which take the same spectral profile, whereas in the cw counterpart, the population distribution is clearly different for each one of those groups. By unifying the MW spectrum for all the groups, the stroboscopic measurement effectively simplifies the dressed MW spectroscopy for the $|m = 0\rangle_x$ state, as in the case of the aligned stretched state.

B. Microwave spectroscopy probing the $F = 1$ state

Figure 8 shows the case of synchronous MW spectroscopy for the $F = 1$ manifold. One can notice the prominence of the extreme peaks in each group. However, the low atomic population in $F = 1$ reduces the signal-to-noise ratio, and a slight propagation effect is noticeable, consistent with the observations for $F = 2$. Nevertheless, these observations indicate that state characterization can be performed in both manifolds $F = 1$ and $F = 2$. Additionally, the model allows for the exploration of different scenarios, such as microwave spectroscopy with arbitrary MW polarization and pump amplitude modulations.

C. Theoretical analysis of microwave spectroscopy for clock, oriented, and aligned states

An additional comparison can be made using the theoretical model. A synchronously dressed, oriented state in an rf magnetic field results in atomically modulated birefringence at twice the modulation frequency of the dressing field. This is analogous to the atomically modulated birefringence observed in the state with alignment [26]. Figure 9 shows the pulsed MW spectra for the three distinct states considering the ideal case, where propagation-induced rotation effects are negligible. Note that the stroboscopic spectroscopy can give access to atomic population distributions according to each input state, e.g., two extreme peaks for the mixture $|F =$

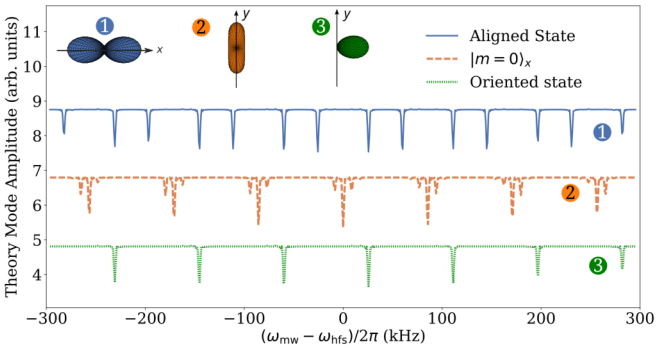

FIG. 9. Theoretical dressed microwave spectra of the Re(m_2) mode amplitude as a function of the microwave frequency detuning. Here the calculated spectra are obtained based on the sequence in Fig. 7 where the MW interaction is stroboscopic and no propagation effect is considered. Curve 1 (blue top solid line), curve 2 (middle orange dashed line), and curve 3 (green bottom dotted line) represent the MW spectra for the aligned stretched state, the $|m=0\rangle_x$ state, and the oriented state, respectively.

$2, m_F = \pm 2\rangle_x$, the center peak for the state $|F=2, m_F=0\rangle_x$, and one extreme peak for the oriented state $|F=2, m_F=2\rangle_x$. This indicates that, under negligible propagation effects, the stroboscopic MW spectroscopy can be used to measure the atomic population distributions when atoms are dressed by rf fields.

Details of our theoretical model are given Appendix A. Extending the model in Ref. [24], which describes isolated atomic systems, this model describes an atomic medium with pumping and relaxation rates. So far we have just discussed the MW spectra when no transverse static fields are applied, focusing on the high amplitude of the second harmonic. However, the model can also predict the cw and pulsed MW spectrum for the first and higher harmonics in the presence of transverse fields, as described by the magnetic interaction term $\hat{H}_B(t)$ in the total Hamiltonian in Eq. (4). Therefore, the model is quite robust and capable of describing the MW spectroscopy of spins in various scenarios.

In order to experimentally overcome the propagation effects, a shorter cell can be used to reduce the backaction of the pump for relatively high atomic populations. This would induce smaller effective rotations in the beam polarization. Nevertheless, this theoretical model allows us to have satisfactory predictions of the expected stroboscopic spectra and their relation to the prepared input state.

VI. CONCLUSION

We have presented a method of microwave spectroscopy for radio-frequency-dressed states applied to a Voigt-effect-based optically pumped magnetometer in an unshielded situation. We tested two methods for interrogating the ground-state population distribution. In the continuous microwave interaction, we observed the violation of standard selection rules, resulting in multiple microwave transitions among the rf-dressed states in the hyperfine ground-state manifold. Alternatively, we demonstrated that changing the microwave interaction profile to rf-synchronized stroboscopic pulsing overcomes the complex interpretation of the cw spectrum. This technique allows efficient state preparation of aligned states driven by a combination of rf fields and optical pump and repump beams. Additionally, stroboscopic measurements can reveal the influence of the NLZ effect on atomic state preparation by showing frequency shifts in the resonance line spacing in simpler spectroscopy. Furthermore, the state probing method enables a distinction between highly polarized ($P \approx 1$) and low-polarization ($P < 1$) manifold populations. Hence, this work paves the way for further investigations into stroboscopic microwave spectroscopy of the Voigt rotation's first harmonic and how the NLZ shift affects the vector response.

Along with the experimental observations, we proposed a model that considers the interaction with magnetic and microwave fields, showing a satisfactory description of the system. The model shows us that the stroboscopic methods can be extended to different kinds of initial states for the magnetometer. Finally, our proposed approach can be easily extended to radio-frequency-dressed Faraday measurements to map the state population distributions, as well as any other dynamical state preparation processes. This work paves the way towards a new form of dressed state detection and vector field mapping.

ACKNOWLEDGMENTS

This work was funded by Engineering and Physical Sciences Research Council through Grant No. EP/M013294/1 and by São Paulo Research Foundation through Grant No. 2018/03155-9.

APPENDIX A: THEORETICAL DESCRIPTION OF THE SPIN DYNAMICS WITH TIME-DEPENDENT MAGNETIC FIELDS

In this Appendix we present the theoretical description of the evolution of an atomic spin interacting with microwave and radio-frequency magnetic fields, considering decoherence effects governed by Langevin dynamics.

1. Spin dynamics with microwave fields

Consider ^{87}Rb atoms with hyperfine ground states $F=1$ and $F=2$. The free Hamiltonian is given by

$$\hat{H}_0 = \sum_F E_F \hat{\mathbb{I}}_F, \tag{A1}$$

where the partial identity operator is defined as

$$\hat{\mathbb{I}}_F = \sum_{m_F=-F}^{F} |F, m_F\rangle\langle F, m_F|. \tag{A2}$$

We show that the dynamics of the density-matrix elements interacting with the microwave field under the rotating-wave approximation is given by the Liouville equation $\frac{d\tilde{\rho}}{dt} = \frac{i}{\hbar}[\tilde{\rho}, \hat{H}^{\text{eff}}_{\text{MW}}]$, where we have defined $\hat{H}^{\text{eff}}_{\text{MW}} = \hat{H}^{\text{eff}}_0 + \hat{H}_S$ with

$$\hat{H}^{\text{eff}}_0 = \Delta \sum_{m_2} |2, m_2\rangle\langle 2, m_2|, \tag{A3}$$

where Δ corresponds to the frequency detuning of the microwave with respect to the hyperfine clock transition.

In addition, we consider the interaction of the atoms in a ground state with a microwave field given by [24]

$$\hat{H}_{\rm MW}(t) = \frac{\mu_B}{\hbar}(g_I\hat{\mathbf{I}} + g_J\hat{\mathbf{J}})\cdot\mathbf{B}_{\rm MW}(t), \tag{A4}$$

where g_I and g_J are the nuclear and electronic g factors, respectively, with the corresponding angular momentum operators $\hat{\mathbf{I}}$ and $\hat{\mathbf{J}}$. In particular, for alkali-metal atoms, for the ground state ${}^nS_{1/2}$ the orbital angular momentum is $L = 0$; hence we can consider $\hat{\mathbf{J}} = \hat{\mathbf{L}} + \hat{\mathbf{S}} \approx \hat{\mathbf{S}}$. Moreover, $g_I \ll g_S$, which allows us to neglect the nuclear term. Thus, the microwave interaction Hamiltonian reduces to

$$\hat{H}_{\rm MW}(t) = \frac{\mu_B g_S}{\hbar}\hat{\mathbf{S}}\cdot\mathbf{B}_{\rm MW}(t), \tag{A5}$$

where the microwave field is described classically in the form

$$\mathbf{B}_{\rm MW}(t) = \tilde{\mathbf{B}}_{\rm MW}e^{-i\omega_{\rm MW}t} + \tilde{\mathbf{B}}^*_{\rm MW}e^{i\omega_{\rm MW}t}, \tag{A6}$$

with polarization $\tilde{\mathbf{B}}_{\rm MW}$ and frequency $\omega_{\rm MW}$. The microwave field can be expressed in the spherical basis as

$$\tilde{\mathbf{B}}_{\rm MW} = \beta^0_{\rm MW}\mathbf{e}_0 + \beta^+_{\rm MW}\mathbf{e}_+ + \beta^-_{\rm MW}\mathbf{e}_-, \tag{A7}$$

where $\mathbf{e}_0 = \mathbf{e}_z$, $\mathbf{e}_\pm = \mp(\mathbf{e}_x + i\mathbf{e}_y)/\sqrt{2}$, and the magnetic-field amplitudes are $\beta^0_{\rm MW} = \beta_{{\rm MW}z}$ and $\beta^\pm_{\rm MW} = \mp(\beta_{{\rm MW}x} \pm i\beta_{{\rm MW}y})$. Therefore, the dynamics given by the Liouville equation is

$$\frac{d\hat{\rho}}{dt} = \frac{i}{\hbar}[\hat{\rho}, \hat{H}_0 + \hat{H}_{\rm MW}(t)], \tag{A8}$$

in which its elements are $\rho_{Fm,F'm'} = \langle Fm|\hat{\rho}|F'm'\rangle$, where $F, F' \in \{1, 2\}$. Transforming into the rotating frame $\tilde{\rho}_{Fm,F'm'} = \rho_{Fm,F'm'}e^{i(F-F')\omega_{\rm MW}t}$, we show that, as in the manifold, the two-level optical system [29] can be expressed in the rotating frame as

$$\begin{aligned}\frac{d\tilde{\rho}_{\alpha m_\alpha,\beta m_\beta}}{dt} &= i(\alpha-\beta)\Delta\tilde{\rho}_{\alpha m_\alpha,\beta m_\beta}\\ &+ i\delta_{F'\beta}\sum_{m,q}\Omega^q_{Fm,F'm_\beta}\tilde{\rho}_{\alpha m_\alpha Fm}\\ &- i\delta_{\alpha F}\sum_{m',q}\Omega^q_{Fm_\alpha,F'm'}\tilde{\rho}_{F'm'\beta m_\beta}\\ &+ i\delta_{F\beta}\sum_{m',q}\Omega^q_{F'm',Fm_\beta}\tilde{\rho}_{\alpha m_\alpha F'm'}\\ &- i\delta_{\alpha F'}\sum_{m,q}\Omega^q_{F'm_\alpha,Fm}\tilde{\rho}_{Fm\beta m_\beta},\end{aligned} \tag{A9}$$

where we have defined the microwave detuning as $\Delta = E_2 - E_1 - \omega_{\rm MW}$ and the Rabi frequencies as

$$\Omega^q_{Fm,F'm'} = \frac{\mu_B g_S}{\hbar}\frac{\mu^q_{Fma,F'mb}}{\hbar}\beta^q_{\rm MW}, \tag{A10}$$

with $\mu^q_{Fm,F'mF'} = \langle F, m_F|\hat{S}^q|F', m'_F\rangle$. The dynamics can be written in terms of an effective Hamiltonian as

$$\frac{d\tilde{\rho}}{dt} = \frac{i}{\hbar}[\tilde{\rho}, \hat{H}^{\rm eff}_{\rm MW}], \tag{A11}$$

where we have defined $\hat{H}^{\rm eff}_{\rm MW} = \hat{H}^{\rm eff}_0 + \hat{H}_S$ with

$$\hat{H}^{\rm eff}_0 = -\begin{bmatrix}0&0&0&0&0&0&0&0\\0&0&0&0&0&0&0&0\\0&0&0&0&0&0&0&0\\0&0&0&\Delta&0&0&0&0\\0&0&0&0&\Delta&0&0&0\\0&0&0&0&0&\Delta&0&0\\0&0&0&0&0&0&\Delta&0\\0&0&0&0&0&0&0&\Delta\end{bmatrix}, \tag{A12}$$

whereas the microwave field Hamiltonian can be expressed as

$$\hat{H}_S = \Omega_\pi\hat{S}_z + \Omega_{\sigma+}\hat{S}_{\sigma+} + \Omega_{\sigma-}\hat{S}_{\sigma-}, \tag{A13}$$

where the longitudinal spin operator is

$$\hat{S}_z = \begin{bmatrix}0&0&0&0&\frac{\sqrt{3}}{4}&0&0&0\\0&0&0&0&0&\frac{1}{2}&0&0\\0&0&0&0&0&0&\frac{\sqrt{3}}{4}&0\\0&0&0&0&0&0&0&0\\\frac{\sqrt{3}}{4}&0&0&0&0&0&0&0\\0&\frac{1}{2}&0&0&0&0&0&0\\0&0&\frac{\sqrt{3}}{4}&0&0&0&0&0\\0&0&0&0&0&0&0&0\end{bmatrix}, \tag{A14}$$

the circular positive operator is

$$\hat{S}_{\sigma_+} = \begin{bmatrix}0&0&0&\frac{\sqrt{3}}{2}&0&0&0&0\\0&0&0&0&\frac{\sqrt{6}}{4}&0&0&0\\0&0&0&0&0&\frac{\sqrt{2}}{4}&0&0\\0&0&0&0&0&0&&\\0&0&0&0&0&0&0&0\\-\frac{\sqrt{2}}{4}&0&0&0&0&0&0&0\\0&-\frac{\sqrt{6}}{4}&0&0&0&0&0&0\\0&0&-\frac{\sqrt{3}}{2}&0&0&0&0&0\end{bmatrix}, \tag{A15}$$

and the negative circular operator is

$$\hat{S}_{\sigma_-} = \begin{bmatrix}0&0&0&0&0&-\frac{\sqrt{2}}{4}&0&0\\0&0&0&0&0&0&-\frac{\sqrt{6}}{4}&0\\0&0&0&0&0&0&0&-\frac{\sqrt{3}}{2}\\\frac{\sqrt{3}}{2}&0&0&0&0&0&0&0\\0&\frac{\sqrt{6}}{4}&0&0&0&0&0&0\\0&0&\frac{\sqrt{2}}{4}&0&0&0&0&0\\0&0&0&0&0&0&0&0\\0&0&0&0&0&0&0&0\end{bmatrix}. \tag{A16}$$

The dynamics describes the Rabi oscillations induced by the microwave field coupling the two hyperfine ground states of alkali-metal atoms.

2. Spin dynamics with radio-frequency fields

Now we add the interaction of atoms with a radio-frequency-dressing field and external static fields

$$\mathbf{B} = \left(B_{\rm rf}\cos\omega_{\rm rf}t + B^{\rm ext}_x\right)\mathbf{e}_x + B^{\rm ext}_y\mathbf{e}_y + \left(B_{\rm dc} + B^{\rm ext}_z\right)\mathbf{e}_z, \tag{A17}$$

where $B_{\rm rf}$ and ω_r are the amplitude and frequency of the rf driving field and $B_{\rm dc}$ is the static field in the longitudinal direction, which are experimentally controlled. Additionally, we have the external fields $B_i^{\rm ext}$ with $i = x$, y, and z, which originate from external sources. Therefore, the magnetic-field interaction is given by $\hat{H}_B = (\mu_B g_F/\hbar)\hat{\mathbf{F}}\cdot\mathbf{B}$, where μ_B and g_F correspond to the Bohr magnetron and g_F factor, respectively, such that

$$\hat{H}_B(t) = [\Omega_{\rm rf}\cos(\omega_{\rm rf}t) + \Omega_x^{\rm ext}]\hat{F}_x + \Omega_y^{\rm ext}\hat{F}_y + \left(\Omega_{\rm dc} + \Omega_z^{\rm ext}\right)\hat{F}_z, \tag{A18}$$

with $g'_F = g_F/\hbar$ and $\Omega_i = \mu_B g'_F B_i$, where $i = {\rm rf}$, dc, x, y, and z. Therefore, the total interaction of the atoms with the microwave and the external magnetic fields dressed by the rf is described by the Hamiltonian

$$\hat{H}_T(t) = \hat{H}_{\rm MW}^{\rm eff} + \hat{H}_B(t). \tag{A19}$$

In addition to this term, which contributes to the coherent dynamics, we need to include the relaxation term, which models atom-atom collisions and atom-wall collisions, and the pumping rate, which describes the state preparation by an pump beam. To do so, we introduce the standard input-output dynamics such that

$$\frac{d\tilde{\rho}}{dt} = \frac{i}{\hbar}[\tilde{\rho}, \hat{H}_T(t)] - \Gamma_p(t)(\tilde{\rho} - \rho_{\rm in}) - \gamma(\tilde{\rho} - \rho_0), \tag{A20}$$

where $\Gamma_p(t)$ corresponds to the pumping rate, which in general can be time dependent (for instance, the amplitude modulation employed to do the state preparation), and γ represents the relaxation rate due to collisions.

For the eight levels of the two hyperfine ground states, we can describe the dynamics above in the Liouville space, as in the case of Ref. [26], by defining $\mathbf{X} = (\tilde{\rho}_{11}, \tilde{\rho}_{12}, \ldots, \tilde{\rho}_{88})$ with dimension $d_\rho = 64$ such that

$$\frac{d\mathbf{X}(t)}{dt} = [\mathbf{M}(t) - \Gamma_p(t) - \gamma]\mathbf{X}(t) + \Gamma_p(t)\mathbf{X}_{\rm in} + \gamma\mathbb{X}_0, \tag{A21}$$

where

$$\mathbf{M}(t) = \mathcal{L}\big[\hat{H}_{\rm MW}^{\rm eff} + \hat{H}_B(t)\big] + \mathcal{R}\big[\hat{H}_{\rm MW}^{\rm eff} + \hat{H}_B(t)\big], \tag{A22}$$

in which $\mathcal{L}(\hat{O})$ and $\mathcal{R}(\hat{O})$ represent the action of the operator $\hat{O}$ to the left and to the right, respectively.

The dynamics of the radio-frequency-dressed states is dominated by the time dependence of rf-driving field $\mathbf{M}(t)$ and the amplitude modulation of the synchronous pumping determined by $\Gamma_p(t)$. On the one hand, since the magnetic field in Eq. (A17) can be harmonically decomposed as $\mathbf{B}(t) = \mathbf{B}^{(0)} + \mathbf{B}^{(1)}e^{i\omega_{\rm rf}t} + \mathbf{B}^{(-1)}e^{-i\omega_{\rm rf}t}$, the magnetic interaction in Eq. (A18) can be also written as

$$\mathbf{M}(t) = \mathbf{M}^{(0)} + \mathbf{M}^{(1)}e^{i\omega_{\rm rf}t} + \mathbf{M}^{(-1)}e^{-i\omega_{\rm rf}t}. \tag{A23}$$

Similarly, when the pump amplitude is modulated, for instance, as a square-wave signal, the pumping rate is decomposed as

$$\Gamma_p(t) = \Gamma_p^{(0)} + \Gamma_p^{(1)}e^{i\omega_{\rm rf}t} + \Gamma_p^{(-1)}e^{-i\omega_{\rm rf}t} + \Gamma_p^{(2)}e^{2i\omega_{\rm rf}t} + \Gamma_p^{(-2)}e^{-2i\omega_{\rm rf}t} + \cdots \tag{A24}$$

such that

$$\Gamma_p^{(0)} = \Gamma_b d, \quad \Gamma_p^{(n)} = \Gamma^{(-n)} = \frac{\Gamma_b}{n\pi}\sin(n\pi d), \tag{A25}$$

where d corresponds to the duty cycle of the carrier wave. The general description in Eq. (A24) can simulate a broad range of time-dependent pumping rates with different spectral decomposition, e.g., sine or sawtooth. This harmonic decomposition of the dynamics generator leads to a Floquet expansion to obtain a stationary solutions of its harmonics [26]. In the next section we present a brief description of the Floquet expansion in order to find the solution of the atomic dynamics.

3. Floquet expansion

Given the harmonic feature of the dynamics generator, one can assume that the solution of the atomic state can be expressed in terms of the Floquet expansion $\mathbf{X}(t) = \sum_n \mathbf{X}^{(n)}(t)e^{in\omega_{\rm rf}t}$ so that one has to determine the amplitude of the harmonics $\mathbf{X}^{(n)}(t)$ to obtain the complete solution. Substituting this expansion into Eq. (A21) yields the recursive formula, which can be written in matrix form as

$$\frac{d\mathbb{X}_F(t)}{dt} = [\tilde{\mathbb{C}} - \mathbb{\Gamma}]\mathbb{X}_F + \mathbb{\Gamma}_{\rm in}\mathbb{X}_{\rm in} + \mathbb{\Lambda}_{\rm rel}\mathbb{X}_0, \tag{A26}$$

where $\mathbb{X}_F = (\mathbf{X}^{(-Q)}, \ldots, \mathbf{X}^{(-n)}, \ldots, \mathbf{X}^{(-1)}, \mathbf{X}^{(0)}, \mathbf{X}^{(1)}, \ldots, \mathbf{X}^{(n)}, \ldots, \mathbf{X}^{(Q)})^T$ corresponds to the vector of harmonic amplitudes of the spin, with cutting frequency Q, and the dynamics generators are

$$\tilde{\mathbb{C}}_{nm} = \begin{cases} \mathbf{C}^{(0)} - in\omega_{\rm rf}\mathbf{I} & \text{for } n = m \\ \mathbf{C}^{(\pm 1)} & \text{for } m = n \mp 1 \\ 0 & \text{otherwise,} \end{cases} \tag{A27}$$

whereas the pump matrix elements $(\mathbb{\Gamma})_{nm} = \Gamma_p^{(n-m)}\mathbf{I}_{3\times 3}$ and

$$(\mathbb{\Gamma}_{\rm in})_{nm} = \begin{cases} \Gamma_p^{(n)}\mathbf{I}_{3\times 3} & \text{for } n = m \\ 0 & \text{otherwise,} \end{cases} \tag{A28}$$

with the input vector $(\mathbb{P}_{\rm in})_n = \mathbf{P}^{\rm in}$.

The magnetometer microwave spectrum has three stages, i.e., synchronous pumping, microwave interaction, and probing, which are shown schematically in Fig. 2. Each sequence is characterized by the equation of motion

$$\frac{d\mathbb{X}_F(t)}{dt} = \begin{cases} [\tilde{\mathbb{C}}_0 - \mathbb{\Gamma}_T]\mathbb{X}_F + \mathbb{\Gamma}_{\rm in}\mathbb{X}_{\rm in} + \mathbb{\Lambda}_{\rm rel}\mathbb{X}_0 & \text{(pump cycle)} \\ [\tilde{\mathbb{C}} - \mathbb{\Lambda}_{\rm rel}]\mathbb{X}_F + \mathbb{\Lambda}_{\rm rel}\mathbb{X}_0 & \text{(MW cycle)} \\ [\tilde{\mathbb{C}}_0 - \mathbb{\Lambda}_{\rm rel}]\mathbb{X}_F + \mathbb{\Lambda}_{\rm rel}\mathbb{X}_0 & \text{(probe cycle),} \end{cases} \tag{A29}$$

where we have defined $\tilde{\mathbb{C}}_0 = \tilde{\mathbb{C}}(H_{\rm MW} = 0)$. During the pumping stage, as before, a steady state is reached. This is given by

$$\mathbb{X}_F^{\rm pump} = -[\tilde{\mathbb{C}}_0 - \mathbb{\Gamma}_T]^{-1}(\mathbb{\Gamma}_{\rm in}\mathbb{X}_{\rm in} + \mathbb{\Lambda}_{\rm rel}\mathbb{X}_0). \tag{A30}$$

After reaching the steady state, the pump pulse is switched off, which is immediately followed by an application of a

microwave pulse. During the microwave cycle, the time evolution is

$$\mathbb{X}_F^{\mathrm{MW}}(t) = e^{(\tilde{\mathbb{C}}_{\mathrm{MW}}-\mathbb{\Lambda}_{\mathrm{rel}})t}\mathbb{X}_F^{\mathrm{pump}} + (\tilde{\mathbb{C}}_{\mathrm{MW}} - \mathbb{\Lambda}_{\mathrm{rel}})^{-1}(e^{(\tilde{\mathbb{C}}_{\mathrm{MW}}-\mathbb{\Lambda}_{\mathrm{rel}})t} - \mathbb{I})\mathbb{\Lambda}_{\mathrm{rel}}\mathbb{X}_0. \tag{A31}$$

If the microwave is continuously interacting for an integer number of rf cycles $t_{\mathrm{MW}} = n/\omega_{\mathrm{rf}}$, then the state at a later time is simply $\mathbb{X}_F^{\mathrm{MW}}(t_{\mathrm{MW}})$. After the microwave pulse, a probe pulse is applied for a given time duration t_{probe}. During the probing, the solution is

$$\mathbb{X}_F^{\mathrm{probe}}(t) = e^{(\tilde{\mathbb{C}}-\mathbb{\Lambda}_{\mathrm{rel}})t}\mathbb{X}_F^{\mathrm{MW}}(t_{\mathrm{MW}}) + (\tilde{\mathbb{C}} - \mathbb{\Lambda}_{\mathrm{rel}})^{-1}(e^{(\tilde{\mathbb{C}}-\mathbb{\Lambda}_{\mathrm{rel}})t} - \mathbb{I})\mathbb{\Lambda}_{\mathrm{rel}}\mathbb{X}_0. \tag{A32}$$

4. Harmonic expansion of the ellipticity

Equation (A32) is the solution from which we can determine the slowly varying envelopes for the Voigt rotation

$$\langle\hat{S}_z'(t)\rangle = \langle\hat{S}_z(t)\rangle + G_F^{(2)}S_y n_F\langle\hat{F}_x^2(t) - \hat{F}_y^2(t)\rangle, \tag{A33}$$

with its dynamics described by the second harmonic in the limit when no transverse fields are applied [20]. According to Eq. (1), when the probe has no initial ellipticity, the Voigt rotations for the ground states $F = 1$ and $F = 2$ are

$$\langle\hat{S}_z'(t)\rangle_{F=1} = G_F^{(2)}S_y n_F[\,\rho_{13}(t) + \rho_{31}(t)], \tag{A34}$$

$$\langle\hat{S}_z'(t)\rangle_{F=2} = G_F^{(2)}S_y n_F\{\sqrt{6}[\rho_{46}(t) + \rho_{64}(t)] + \sqrt{6}[\rho_{68}(t) + \rho_{86}(t)] + 3[\rho_{75}(t) + \rho_{57}(t)]\}, \tag{A35}$$

where each term has a spectral expansion of the form $\rho_{ij}(t) = \rho_{ij}^{(0)}(t) + \rho_{ij}^{(1)}(t)e^{i\omega_{\mathrm{rf}}t} + \rho_{ij}^{(2)}(t)e^{2i\omega_{\mathrm{rf}}t} + \cdots + \mathrm{c.c.}$ Thus, by extracting the mode amplitude of the second harmonic in Eq. (A32),

$$\mathbf{X}_R^{(2)} = \frac{1}{2T}\int_0^T dt'\{[\mathbb{X}_F^{\mathrm{probe}}(t')]_2 + [\mathbb{X}_F^{\mathrm{probe}}(t')]_{-2}\}, \tag{A36}$$

we can express the ellipticities in Eq. (A35) in terms of the solution in Eq. (A36), since the second-harmonic matrix elements are $\rho_{ij}^{(2)}(t) = [\mathbf{X}_R^{(2)}]_{d_\rho\times i+j}$.

APPENDIX B: DETAILS OF THE EXPERIMENTAL SETUP

Here we present some more details of our magnetically unshielded experimental setup depicted in Fig. 1(a), a paraffin-coated ^{87}Rb enriched vapor cell of diameter $d =$ 26 mm and length $l = 75$ mm at room temperature, with a density of approximately 10^{10} atoms per cubic cm. The atomic state is dressed with a radio-frequency field which is generated by a cosine-theta coil along the x axis. The atoms are dressed with an $\omega_{\mathrm{rf}} = 2\pi \times 90$ kHz rf field and and coupled to a static field in the longitudinal direction. Three Helmholtz coils are used to actively compensate and stabilize the external magnetic field using an analog three-channel proportional-integral-derivative controller driving a homemade bipolar current source. The in-loop field is sensed by a three-axis fluxgate magnetometer (Stefan-Mayer FLC3-70). The atomic state is prepared by a combination of copropagating linearly polarized pump laser beams tuned to the $F = 2$ to $F' = 1$ transition of the $D1$ line and a linearly polarized repump laser tuned to the $F = 1$ to $F' = 2$ transition of the $D2$ line. The atoms are stroboscopically pumped by modulating the pump amplitude with a 10% duty cycle in phase with the rf field with the repump set in the cw mode.

For a complete characterization of the atomic state, we employ the Voigt rotation as a nondestructive measurement to probe the atoms in hyperfine ground states $F = 1$ and $F = 2$. To do so, the atoms are probed by a 45° polarized laser beam relative to the pump polarization and tuned −500 MHz with respect to the $F = 2$ to $F' = 1$ transition and $F = 1$ to $F' = 1$ transition of the D1 line. After the interaction with the atoms, the light passes through a quarter waveplate and a polarizing beam splitter, which allows us to measure the Voigt rotation of the light polarization, i.e., the ellipticity induced by the atoms. The light is detected on a balanced photodetector, which is amplified (ZFL-500+) and split (ZSC-3-2+) such that the signals are mixed (ZAD-3+) with the rf-field signal, where the detected signal $u(t) = g_{\mathrm{el}}S_z(t)$ is proportional to the ellipticity in Eq. (1) and the electronic gain g_{el}. As it was shown in Ref. [20], the ellipticity for the Voigt rotation produces a signal at the first and second harmonics of the radio-frequency-dressing field such that $u(t) = m_0 + m_1e^{i\omega_{\mathrm{rf}}t} + m_2e^{2i\omega_{\mathrm{rf}}t} + \mathrm{c.c.}$ This output signal is demodulated at the second harmonic using a homebuilt in-phase–quadrature demodulator, from which we can extract its mode amplitude m_2.

The microwave spectroscopy is performed when the magnetometer is tuned on the resonance $B_z = \hbar\omega_{\mathrm{rf}}/\mu_B g_F$ of the second harmonic of the Voigt rotation, canceling the presence of any transverse field, i.e., zeroing the first harmonic [20]. The microwave field is generated using an rf generator (SRS SG380) with a frequency doubler (Minicircuits ZX90-2-36-S+) and an additional amplifier. The signal is coupled into a half-wave dipole antenna $L = \lambda/2 = 21.9$ mm, where L is the conductor length and λ corresponds to the $|F = 1\rangle \rightarrow |F = 2\rangle$ hyperfine microwave transition. The direction of the dipole antenna is transverse to the light propagation.

APPENDIX C: STATE ROTATION

According to Ref. [30], the rotation of a state represented by the density matrix ρ is given by

$$\rho' = \mathcal{D}\rho\mathcal{D}^\dagger, \tag{C1}$$

where $\mathcal{D}$ is the rotation operator. The rotation of a density matrix about the z axis by an angle ϕ is given by

$$[\mathcal{D}_z(\phi)]_{mm'} = e^{-im\phi}\delta_{mm'}. \tag{C2}$$

Then the density matrix resulting from the rotation is given by

$$\rho'_{mm'} = e^{-im\phi}\rho_{mm'}e^{-im'\phi} = e^{-i(m-m')\phi}\rho_{mm'}. \tag{C3}$$

With this rotation we emulate state preparation of an effective rotated pump field.

[1] D. Budker and M. Romalis, Nat. Phys. **3**, 227 (2007).
[2] D. Budker and D. F. J. Kimball, *Optical Magnetometry* (Cambridge University Press, Cambridge, 2013).
[3] S. A. Murthy, D. Krause, Jr., Z. L. Li, and L. R. Hunter, Phys. Rev. Lett. **63**, 965 (1989).
[4] M. V. Romalis, W. C. Griffith, J. P. Jacobs, and E. N. Fortson, Phys. Rev. Lett. **86**, 2505 (2001).
[5] H. Xia, A. Ben-Amar Baranga, D. Hoffman, and M. V. Romalis, Appl. Phys. Lett. **89**, 211104 (2006).
[6] E. Boto, N. Holmes, J. Leggett, G. Roberts, V. Shah, S. S. Meyer, L. D. Muñoz, K. J. Mullinger, T. M. Tierney, S. Bestmann, G. R. Barnes, R. Bowtell, and M. J. Brookes, Nature (London) **555**, 657 (2018).
[7] K. Jensen, R. Budvytyte, R. A. Thomas, T. Wang, A. M. Fuchs, M. V. Balabas, G. Vasilakis, L. D. Mosgaard, H. C. Stærkind, J. H. Müller, T. Heimburg, S.-P. Olesen, and E. S. Polzik, Sci. Rep. **6**, 29638 (2016).
[8] R. Fenici, D. Brisinda, and A. M. Meloni, Exp. Rev. Mol. Diagn. **5**, 291 (2005).
[9] R. Wyllie, M. Kauer, R. T. Wakai, and T. G. Walker, Opt. Lett. **37**, 2247 (2012).
[10] J. C. Allred, R. N. Lyman, T. W. Kornack, and M. V. Romalis, Phys. Rev. Lett. **89**, 130801 (2002).
[11] H. B. Dang, A. C. Maloof, and M. V. Romalis, Appl. Phys. Lett. **97**, 151110 (2010).
[12] A. Ben-Kish and M. V. Romalis, Phys. Rev. Lett. **105**, 193601 (2010).
[13] W. Lee, V. G. Lucivero, M. V. Romalis, M. E. Limes, E. L. Foley, and T. W. Kornack, Phys. Rev. A **103**, 063103 (2021).
[14] G. Bao, A. Wickenbrock, S. Rochester, W. Zhang, and D. Budker, Phys. Rev. Lett. **120**, 033202 (2018).
[15] R. Zhang, D. Kanta, A. Wickenbrock, H. Guo, and D. Budker, Phys. Rev. Lett. **130**, 153601 (2023).
[16] S. Groeger, G. Bison, J.-L. Schenker, R. Wynands, and A. Weis, Eur. Phys. J. D **38**, 239 (2006).
[17] D. Arnold, S. Siegel, E. Grisanti, J. Wrachtrup, and I. Gerhardt, Rev. Sci. Instrum. **88**, 023103 (2017).
[18] M. Ranjbaran, M. M. Tehranchi, S. M. Hamidi, and S. M. H. Khalkhali, J. Magn. Magn. Mater. **441**, 718 (2017).
[19] A. Weis, G. Bison, and A. S. Pazgalev, Phys. Rev. A **74**, 033401 (2006).
[20] T. Pyragius, H. M. Florez, and T. Fernholz, Phys. Rev. A **100**, 023416 (2019).
[21] C. Kiehl, D. Wagner, T.-W. Hsu, S. Knappe, C. A. Regal, and T. Thiele, Phys. Rev. Res. **5**, L012002 (2023).
[22] C. Kiehl, T. S. Menon, S. Knappe, T. Thiele, and C. A. Regal, Phys. Rev. Appl. **22**, 014005 (2024).
[23] B. P. Masterson, C. Tanner, H. Patrick, and C. E. Wieman, Phys. Rev. A **47**, 2139 (1993).
[24] G. A. Sinuco-Leon, B. M. Garraway, H. Mas, S. Pandey, G. Vasilakis, V. Bolpasi, W. von Klitzing, B. Foxon, S. Jammi, K. Poulios, and T. Fernholz, Phys. Rev. A **100**, 053416 (2019).
[25] B. Julsgaard, J. Sherson, J. L. Sørensen, and E. S. Polzik, J. Opt. B **6**, 5 (2004).
[26] H. M. Florez and T. Pyragius, Phys. Rev. A **103**, 033113 (2021).
[27] S. Jammi, T. Pyragius, M. G. Bason, H. M. Florez, and T. Fernholz, Phys. Rev. A **97**, 043416 (2018).
[28] D. Budker, W. Gawlik, D. F. Kimball, S. M. Rochester, V. V. Yashchuk, and A. Weis, Rev. Mod. Phys. **74**, 1153 (2002).
[29] D. A. Steck, Rubidium 87 D Line Data, available at http://steck.us/alkalidata (2015), version 2.1.5.
[30] D. Budker, M. Auzinsh, and S. Rochester, *Optically Polarized Atoms: Understanding Light-atom Interactions* (Oxford University Press, Oxford, 2014).